The search for an antiviral lead molecule to combat the neglected emerging Oropouche virus

Rafaela dos Santos Peinado [a,1], Marielena Vogel Saivish [b,c,1], Gabriela de Lima Menezes [d,1], Umberto Laino Fulco [d], Roosevelt Alves da Silva [e], Karolina Korostov [f], Raphael Josef Eberle [f,g], Paulo A. Melo [h], Maurício Lacerda Nogueira [b,i], Carolina Colombelli Pacca [b], Raghuvir Krishnaswamy Arni [a], Mônika Aparecida Coronado [a,f,*]

[a] *Multiuser Center for Biomolecular Innovation, Departament of Physics, Instituto de Biociências Letras e Ciências Exatas (Ibilce), Universidade Estadual Paulista (UNESP), São Jose do Rio Preto-SP 15054-000, Brazil*
[b] *Laboratórios de Pesquisas em Virologia, Departamento de Doenças Dermatológicas, Infecciosas e Parasitárias, Faculdade de Medicina de São José do Rio Preto, São José do Rio Preto, SP 15090-000, Brazil*
[c] *Brazilian Biosciences National Laboratory, Centro Nacional de Pesquisa em Energia e Materiais (CNPEM), Campinas, SP 13083-100, Brazil*
[d] *Bioinformatics Multidisciplinary Environment, Programa de Pós Graduação em Bioinformática, Universidade Federal do Rio Grande do Norte, Natal 59078-400, RN, Brazil*
[e] *Núcleo Colaborativo de Biosistemas, Universidade Federal de Jataí, Jataí 75801-615, GO, Brazil*
[f] *Institute of Biological Information Processing (IBI-7: Structural Biochemistry), Forschungszentrum Jülich, Jülich 52428, Germany*
[g] *Institut für Physikalische Biologie, Heinrich-Heine-Universität Düsseldorf, Universitätsstraße, Düsseldorf 40225, Germany*
[h] *Departamento de Farmacologia Básica e Clínica - ICB, CCS, Universidade Federal do Rio de Janeiro, Rio de Janeiro, RJ 21941-590, Brazil*
[i] *Sealy Center for Vector-Borne and Zoonotic Diseases, The University of Texas Medical Branch, Galveston, TX 77555-0609, USA*

ARTICLE INFO

ABSTRACT

Oropouche virus (OROV) is a member of the *Peribunyaviridae* family and the causative agent of a dengue-like febrile illness transmitted by mosquitoes. Although mild symptoms generally occur, complications such as encephalitis and meningitis may develop. A lack of proper diagnosis, makes it a potential candidate for new epidemics and outbreaks like other known arboviruses such as Dengue, Yellow Fever and Zika virus. The study of natural molecules as potential antiviral compounds is a promising alternative for antiviral therapies. Wedelolactone (WDL) has been demonstrated to inhibit some viral proteins and virus replication, making it useful to target a wide range of viruses. In this study, we report the *in silico* effects of WDL on the OROV N-terminal polymerase and its potential inhibitory effects on several steps of viral infection in mammalian cells *in vitro*, which revealed that WDL indeed acts as a potential inhibitor molecule against OROV infection.

1. Introduction

Oropouche virus (OROV) is the causative agent of Oropouche fever - an acute febrile disease that affects humans, with symptoms such as fever, joint pain, skin rash and headaches that may also develop diseases such as meningitis or encephalitis (Sakkas et al., 2018). Transmission occurs by the bite of infected *Culicoides paraensis* midges; however, its first isolation occurred in 1955 from a human case in the village of Vega de Oropouche in Trinidad related to *Coquilletidia venezuelensis* mosquitoes (Anderson et al., 1961). OROV belongs to the *Peribunyaviridae* family and the *Orthobunyavirus* genus, and its prevalence in the Americas, especially in Central and South Americas, has made it a potential candidate for epidemics and outbreaks along with other arboviruses like Dengue, Zika, Chikungunya and Mayaro (Romero-Alvarez and Escobar, 2018). In Brazil, it was first isolated in 1960 from a sloth (*Bradypus tridactylus*) near the Belem-Brasilia highway construction sites and from *Ochlerotatus serratus* mosquitoes nearby. Since then, several outbreaks have been reported with high infection numbers (Vasconcelos et al., 2011).

The OROV viral particle is known to be spherical and measures

---

* Corresponding author at: Institute of Biological Information Processing (IBI-7: Structural Biochemistry), Forschungszentrum Jülich, Jülich, 52428, Germany.
E-mail address: monikacoronado@gmail.com (M.A. Coronado).
[1] These authors contributed equally to this work.

approximately 110 nm in diameter. It is characterised by the three-segmented negative sense genomic RNAs that are linked to the viral RNA-dependent RNA polymerase (L protein) and surrounded by the nucleocapsid protein (N) (Travassos da Rosa et al., 2017). The three genomic segments are known as small (S), medium (M) and large (L), related to their molecular sizes, and they are flanked by two terminal non-coding regions (NCRs) in the 5′ and 3′ ends that seem to be essential for replication and transcription mechanisms as they are complementary and function as promoters (Travassos da Rosa et al., 2017). The L RNA segment comprises one ORF (open reading frame) that encodes the RNA-dependent RNA polymerase, which is associated to the three RNA segments. The M RNA segment has a single ORF, which encodes the two structural surface glycoproteins Gn and Gc and also the nonstructural NSm protein, which has been demonstrated to be dispensable for replication in mammalian and mosquito cells that lack interferon response, but in some cases, it might play a role in virulence and pathogenesis (Gerrard, et al., 2007; Travassos da Rosa et al., 2017). Lastly, the S RNA segment has two overlapping ORFs that encode the structural nucleocapsid protein and the nonstructural NSs protein, which is an important virulence factor antagonising type I interferon response (Billecocq et al., 2004; Travassos da Rosa et al., 2017).

Despite the knowledge of its epidemiology and geographical distribution and circulation, OROV is still a neglected tropical disease with significant potential to cause future epidemics and spillover events in neotropical areas, especially due to challenges in clinical diagnosis which depends mostly on commercially unavailable serological assays, and therefore, to date, no licensed vaccination is available (Romero-Alvarez and Escobar, 2018), which makes the search for antiviral molecules and their effects on viral infection as well as viral elements an important field to develop future antiviral therapies.

Wedelolactone (WDL), a coumestan derived from *Eclipta prostrata* (*Asteraceae*) (Fig. 1), has demonstrated relevant results against several viruses, including HIV-I (Human immunodeficiency virus) (Tewtrakul et al., 2007), HCV (Hepatitis C virus) (Manvar et al., 2012) and HCMV (Human cytomegalovirus) (Svrlanska et al., 2020) with inhibitory effects on viral proteins as well as on viral replication events.

These results instigated us to evaluate its *in vitro* effects on mammalian cells infected with OROV through antiviral assays, the inhibitory effects on OROV endonuclease, and the mode of interaction using *in silico* experiments (docking and molecular dynamics).

2. Materials and methods

2.1. Cell culture and virus

Vero cells were grown in Minimal Essential Medium (MEM) (Gibco, Waltham, MA, USA) supplemented with 10 % (v/v) heat-inactivated fetal bovine serum (FBS) (Gibco, Waltham, MA, USA), 100 U. mL^{-1} of penicillin, 0.1 mg. mL^{-1} of streptomycin, and 0.5 µg. mL^{-1} of amphotericin B (Gibco, Waltham, MA, USA) and incubated at 37 °C under a humidified atmosphere containing 5 % CO_2. The C6/36 cells were cultured in Leibovitz-15 medium (L-15) with 10 % FBS at 28 °C. Oropouche virus (strain BeAn 19,991) stocks were propagated in C6/36
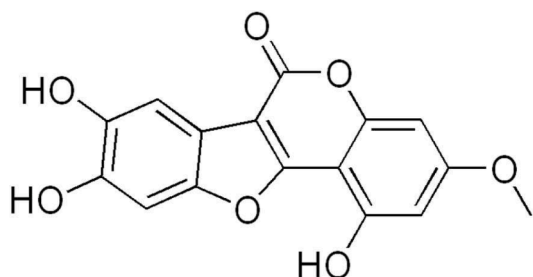

Fig. 1. Wedelolactone chemical structure. Generated by ChemDraw.

cells and titrated in Vero cells using plaque-forming assay (PFU), described below. Wedelolactone ("WDL", 7-methoxy 5,11,12-trihydroxy-coumestan) was purchased from Aktin Chemicals, China (purity ≥ 98 %) and dissolved in DMSO vehicle (dimethyl sulfoxide – 10 mg/mL).

2.2. Cytotoxicity analysis

Vero cells (5×10^4) grown in 96-well plates in MEM were treated with Wedelolactone at concentrations ranging from 50 µM to 400 µM for 48 h, at which point, 1 mg/mL of 3-(4,5-Dimethyl-2-thiazolyl)−2,5-diphenyltetrazolium bromide (MTT, Sigma, Aldrich, Saint Louis, MI, USA) was added to the cells, and incubated for 1 h. Formazan crystals were dissolved in DMSO, and absorbance was determined at 550 nm using a Spectramax Plus Microplate reader (Molecular Devices, Sunnyvale, CA, USA). Results are shown as the percentage of viable cells relative to untreated control cells. All assays were performed three times independently in triplicate. From this, the CC_{50} (cytotoxic concentration of the compound that reduced cell viability to 50 %) was calculated from a dose-response curve in GraphPad Prism (version 8.0) using a four-parameter curve fitting.

2.3. Virus plaque-forming units assay

Briefly, Vero cells grown in a 24-well culture plate were infected by 0.1 mL of ten-fold dilutions of the viral stock. Following incubation of 1 h at 37 °C, 0.5 mL of culture medium supplemented with 2 % fetal bovine serum (FBS) and 1.5 % carboxymethylcellulose sodium salt (Sigma-Aldrich, Saint-Quentin-Fallavier, France) were added, and the incubation was extended for three days at 37 °C. The cells were fixed (formaldehyde 10 %) and stained with 2 % crystal violet diluted in 20 % ethanol after removing the media. Plaques were counted and expressed as plaque-forming units per milliliter (PFU·mL^{-1}) (Lennette, 1995).

2.4. Viral infection assay

To explore which step(s) of the viral lifecycle is blocked by WDL, time-of-drug experiments were performed. The molecule was added to the virus and/or host cells at different time points relative to viral inoculation to the cells: (1) Pre-treatment of virus followed by inoculation of the treated virus to the cells examines the virucidal or neutralising activity of the WDL. (2) Pre-treatment of the cells with WDL before viral inoculation examines whether the substance could block the viral receptor to inhibit viral attachment to the host cells or if it could induce the production of antiviral host factors. (3) Co-treatment of cells and virus during virus inoculation examines the WDL on the virus entry steps blockade of viral attachment and penetration to the cells. (4) Treatment of virus-infected cells during the entire post-inoculation period examines the antiviral effect of Wedelolactone during the post-entry steps, such as genome translation and replication, virion assembly and virion release from the cells. Viral infection experiments were performed in Vero cells seeded in 96-well plates treated with or without Wedelolactone. The cells were infected with a multiplicity of infection (MOI) of 0.1 for OROV for 1 h at 37 °C. Cell supernatants were harvested at the indicated time intervals (12, 24, 48 or 72 hpi) to quantify the viral titers using a plaque-forming assay described above. Three independent experiments were performed. Data were analysed by a four-parameter curve fitting from a dose-response curve using GraphPad Prism (version 8.0) to calculate the EC_{50}. The selectivity index for the compound was determined as the ratio of the CC_{50} to the EC_{50}.

2.5. Cloning

The codon-optimised cDNA encoding the N-terminal endonuclease protein (residues 1–179; GenBank Protein Accession number AJE24678.1) of OROV RNA-polymerase (Endo-Nter) was synthesised

and implemented in the Kanamycin resistant vector pET-24a(+). The construct contains an N-terminal hexahistidine affinity tag and a TEV protease cleavage site.

2.6. Protein expression and purification

Endo-Nter-pET-24a(+) vectors were transformed into *E.coli* Rosetta (DE3) (Novagen) competent cells and grown overnight at 37 °C in SOC medium. The pre-culture was added to fresh LB-medium plus kanamycin and chloramphenicol and grew at 37 °C until the cells reached OD_{600} between 0.6 – 0.8. The culture was induced with 0.5 mM IPTG and incubated for 5 h at 37 °C and 120 rpm. After the cells were harvested, the pellet was dissolved in 3 M Guanidine, 20 mM Tris_HCl, 500 mM NaCl, 1 mM ß-mercaptoethanol, pH 8.0 and incubated at room temperature for 30 min. Subsequently, the dissolved cells were centrifuged at 7000 rpm, 10 °C for 60 min, followed by filtration (0.45 μm) and loaded onto the Ni-NTA column pre-equilibrated with the same buffer. The protein was eluted with 500 mM imidazolium. The eluted fraction was dialysed against 3 M GdmCl, 10 mM Tris–HCl, 100 mM Sodium phosphate, 10 mM ß-mercaptoethanol at pH 8.0 to remove the imidazolium. The protein refolding was performed using 10 mM Tris–HCl, 100 mM Sodium phosphate, and pH 8.0.

2.7. Western blot analysis

Protein samples were prepared in Laemmli buffer (final 1 × composition: 20 mM Tris, pH 6.8, 2 % SDS, 6 % glycerol, 1 % β-ME, 0.002 % Bromophenol Blue). All samples were heated at 95 °C for 5 min and separated using SDS PAGE (15 %). Proteins were then transferred to a polyvinylidene fluoride (PVDF) membrane (Thermo Fisher Scientific, Waltham, USA) at 500 mA for 40 min. After a washing step for 15 min in Tris-buffered saline tween buffer (TBS-T) (20 mM Tris, 150 mM NaCl, 0.1 % Tween 20), the membrane was blocked for 1 h with 2.5 % milk powder/TBS-T. Next, the membrane was washed with TBS-T, 2 × 5 min and in the last step for 15 min. Penta-His-Mouse antibody (Thermo Fisher Scientific, Waltham, USA) stocks were 1 mg/ml and were diluted in TBS-T (1:1000). The membrane was incubated with the antibody for 1.5 h, at RT and washed after 3 × 5 min with TBS-T. Afterwards, the membrane was incubated for 1.5 h, at RT with a Goat anti-Mouse antibody (Thermo Fisher Scientific, Waltham, USA), diluted in TBS-T (1:10,000). Next, the membrane was washed 3 × 5 min with TBS-T. The Goat anti-Mouse antibody is conjugated with horseradish peroxidase (HRP), which mediate the chemiluminescent detection using a HRP detection kit (Thermo Fisher Scientific, Waltham, USA). Bio-Rad universal hood II and Chemidoc XRS camera and Quantity One 4.6.5 software enabled the visualisation and quantification of the protein bands.

2.8. FRET based activity assay

OROV Endo-Nter activity assay was performed as described previously for viral endonucleases (Guo et al., 2012; Noble et al., 2012), using the DNA substrate FAM-TCT CTA GCA GTG GCG CC-TAM (Integrated DNA Technologies, Coralville, USA), at a concentration of 2 μM. The reaction buffer contains 50 mM Hepes pH 7.5, 150 mM KCL and 1 mM MnCL. The assay contained Endo-Nter at a final concentration of 320 nM in 60 μL volume reactions, using an Infinite 200 PRO plate reader (Tecan, Männedorf, Switzerland). For each experiment three controls were conducted, buffer + substrate, buffer + protein and as negative control 1 mM EDTA.

For the determination of the half-maximal inhibitor concentration (IC_{50}) the protein was treated with 0–50 μM WDL and measured directly. All inhibition assays were performed as triplicates, and the results were presented as mean ± standard deviation (SD). The assay was performed in Corning 96-well plates (Merck, Darmstadt, Germany), and the fluorescence intensities were measured at 60 s intervals over 60 min at 37 °C. The excitation and emission wavelengths were 495 nm and 520 nm,

respectively. The IC_{50} value was calculated by plotting the initial velocity against various concentrations of the combined molecules using a dose-response curve in GraphPad Prism 5 software (San Diego, CA, USA), and data are presented as mean ± SD. The inhibition mode of WDL was determined using different final concentrations of the inhibitor (0, 0.05, 0.1, 0.25 and 0.5 μM) and substrate (0, 1, 2, 3, 4 and 5 μM). WDL at various concentrations was added to 320 nM OROV Endo-Nter, and the reaction was directly initiated by the addition of the corresponding concentration series of the substrate. The data were analysed using a Lineweaver-Burk plot; therefore, the reciprocal of velocity (1/V) *vs* the reciprocal of the substrate concentration (1/[S]) was compared (Roy et al., 2017). All measurements were performed in triplicate, and data are presented as mean ± SD. Each activity assay and inhibition mode experiment was performed with freshly purified protein.

2.9. Molecular dynamics (MD) simulations, ensemble docking and binding free energy analysis

2.9.1. model of the OROV Endo-Nter domain

The crystallographic structure of the OROV Endo-Nter is not yet available. Therefore, the N-terminal sequence (1–180) comprising the endonuclease domain of the polymerase protein was retrieved from the GenBank database (accession code: AJE24678) for molecular modelling using I- TASSER server. The coordinates of the initial model were submitted to the MolProbity server (Williams et al., 2018) to assess the model's quality. These results indicate that the protein modelled by I-TASSER has a high-quality conformation suitable for MD simulations. The manganese ion (Mn^{2+}) was inserted into the model by overlaying it with the N-terminal endonuclease structure of *La Crosse* virus (PDB ID: 2XI5) (Reguera et al., 2010), as the output model does not contain the ion. Subsequently, the PropKa server (Olsson et al., 2011) was used to predict the protonation state of the amino acid side chains at pH 7.4.

2.9.2. Molecular dynamic (MD) simulations without ligand

Prior to ligand docking, a molecular dynamics (MD) simulation of the OROV Endo-Nter domain was performed. Three identical systems were prepared and subjected to MD simulations for 200 ns each using GROMACS 2020.3 software (Abraham et al., 2015) with Amber ff99SB-ILDN as a force field. The systems were placed in a cubic box with TIP3P water model extended 12 Å away from solute atoms and neutralised with Na^+ ions. Two rounds of energy minimisation removed bad contacts of the starting structure. The first step consisted of a maximum of 500 steps or when the maximum force in any atom reached a value below 50 kJ/mol/nm, using the steepest descent algorithm with protein restraint, focusing on solvent relaxation. The second minimisation step was performed without protein restraint in flexible water, using the same steepest descent algorithm. In addition, the maximum steps were increased to 10,000 steps or when the force applied in the atom reached a value less than 250 kJ/mol/nm.

The system's pressure and temperature were set to 1 atm and 310 K in two separate 100 ps steps, referred to as the NVT ensemble (temperature setting) and NPT ensemble (pressure setting). For this purpose, the modified Berendsen (Berendsen et al., 1984) and Parrinello-Rahman (Hutter, 2012) algorithms were applied to adjust the system temperature and pressure, respectively. In both steps, bonds with hydrogen were constrained by the LINCS algorithm (Hess et al., 1997) and positional restraints were applied in the protein to equilibrate the solvent around the solute.

The Particle Mesh Ewald summation method was used to calculate long-range electrostatic interactions, and a cut-off of 1 nm was defined for non-bonded interactions. Finally, the leap-frog algorithm (Hockney et al., 1974) was used to integrate the equations of motion, with a time step of 0.2 fs. Before the MD simulation, a small NPT ensemble of 1 ns was performed with no restriction at the protein position. The production run of each identical system was performed at 200 ns with no restriction at protein conformation. A total of 2000 protein frames were

produced from each MD run. Each run is referred to here as a replicate.

The MD trajectories were visualised using UCSF Chimera software (Pettersen et al., 2004). The root means square deviation (RMSD) and fluctuation (RMSF) were calculated using the "gmx" commands of the GROMACS package. All plots were generated using the R language in Rstudio 4.1.1 (RStudio Team, n.d.) and protein image representations were generated in UCSF ChimeraX (Pettersen et al., 2021).

2.9.3. Ensemble docking

AutoDock Vina 1.2.2 software (hereafter referred to as Vina) was used for docking (Trott and Olson, 2009). First, the 3D structure of the ligand, WDL, was retrieved from the PubChem database (https://pubchem.ncbi.nlm.nih.gov/compound/Wedelolactone) in SDF format. The molecule was converted to PDB format using Marvin Sketch software (https://www.chemaxon.com/). OpenBabel software (O'Boyle et al., 2011) was used to convert PDB to PDBQT, setting the pH of the ligand to 7.4.

Ensemble docking was performed using all frames from each MD run. To convert all frames from PDB to PDBQT, the prepare_receptor.py script from the MGLTools package (https://ccsb.scripps.edu/mgltools/) was used. The grid box to delimit the ligand pose search was based on all frames of the trajectory. The binding pocket is the same as the binding of Mn^{2+}, so the grid box was defined as the smallest that encompassed this pocket in all protein frames. The Vina output contained nine binding poses for each frame-ligand docking. The best score (in kcal/mol) for each frame was recorded and analysed in RStudio software.

2.9.4. MM/GBSA and MM/PBSA free energy calculation

Complexes were determined based on Vina docking results. The complexes with the best (lowest) and worst (highest) Vina scores were submitted to MD simulations using the same protocol described above for each replicate. The MD simulations' ligand parameters were determined via the ACPYPE server (https://www.bio2byte.be/acpype/) (Silva and Vranken, 2012) using BCC as the charge method and GAFF2 as the atom type. The server provided all topology and parameter files required for MD simulation using GROMACS software. A total of six MDs (two for each replicate) of the protein-ligand complex were performed. For each MD, the last 500 frames (50 ns) of the complexes were analysed using Molecular Mechanics/Generalized Born and Poisson-Boltzmann surface area (MM/GBSA and MM/PBSA, respectively) free energy calculation, with all solvent molecules and Na^+ ions removed. GB-Neck2 (igb=8) (Nguyen et al., 2013) was used, and the internal dielectric constant was set to 4 (indi=4), which is the most accurate for highly charged binding pockets according to comparative studies (Hou et al., 2011). Besides, per-residue decomposition analyses of MM/PBSA were performed to determine the energetic contribution of each residue, including the Mn^{2+} ion using gmx_MMPBSA (Valdés-Tresanco et al., 2021), which allows performing directly from the output of GROMACS MD simulations to calculate MM/GB(PB)SA. The 2D diagrams of protein-ligand interaction were generated using Discovery Studio Visualizer 2019 from Accelrys (BIOVIA, n.d.).

3. Results and discussion

3.1. Preparation of OROV Endo-Nter

The N-terminal endonuclease-His-tag fusion protein of OROV was expressed in *E. coli* Rosetta (DE3) cells and purified using a Ni-NTA affinity column. The pellet was resuspended in a lysis buffer containing 3 M Guanidine to access the His-Tag. After Ni-NTA purification, the respective fraction was dialysed against the same buffer to remove the imidazolium. Consecutively, the protein was dialysed against 10 mM Tris–HCl, 100 mM Sodium phosphate, pH 8. The 15 % SDS-PAGE gel (Figure S1) indicates the purity of the protein and the western blot analysis showed that the molecular weight of the protein was about 25 kDa (Figure S1).

3.2. OROV Endo-Nter activity assay

Before testing the effect of the selected inhibitor, freshly purified OROV Endo-Nter activity was investigated, using an FRET based assay as described previously for viral endonucleases (Guo et al., 2012; Noble et al., 2012), using 2 μM DNA substrate FAM-TCT CTA GCA GTG GCG CC-TAM (Integrated DNA Technologies, Coralville, USA). Based on the substrate cleavage the increasing fluorescence intensities were measured over 60 min (Figure S2A). Three independent controls (Buffer + substrate, buffer + protein and EDTA) were performed, Buffer + substrate and buffer + protein showed no increasing fluorescence intencities over the experimental time and 1 mM EDTA was used as negative control (Figure S2A and B).

3.3. Inhibition effect of wedelolactone against Orov endonuclease domain

The selected molecule (WDL) was analysed with respect to its ability to inhibit the activity of the Endo-Nter domain, which is essential for transcription, binding and cleaving RNA; however, it is not essential in replication steps (Amroun et al., 2017). The investigated concentration range of $0 - 50$ μM (Fig. 2a) demonstrated that WDL efficiently inhibited the endonuclease activity by 100 % at 25 μM final concentration of WDL, displaying an IC_{50} value of 310 ± 8 nM (Fig. 2b).

Further experiments identified WDL as a competitive inhibitor of the OROV Endo-Nter substrate (Fig. 2c), probably blocking the Mn^{2+} site.

### 3.4. Cytotoxicity effects of wedelolactone in Vero cells

To evaluate the cytotoxic effect of WDL, we set the maximum concentration of the molecule for toxicity assessment to 400 μM of the molecule, displaying cell viability above 50 % at 300 μM. Vero cell toxicity was analysed 48 h post-treatment using an MTT cytotoxicity assay (Kumar et al., 2018). The calculated CC_{50} for WDL was 373.5 ± 154.2 μM using GraphPad Prism 8 software (San Diego, CA, USA) from a normalised dose-response curve fitting (Fig. 3).

### 3.5. Wedelolactone inhibition of OROV replication is concentration-dependent

To evaluate whether OROV progeny reduction is affected by WDL concentration, we treated Vero cells with different molecule concentrations (ranging from 10 to 40 μM) under different treatment conditions, and the viral progeny production was measured. To explore which step(s) of the viral lifecycle is blocked by the molecule, additional time-of-drug experiments were performed, as described in the methods section. In brief, the molecule was added to the virus and/or host cells at different time points relative to viral inoculation to the cells. Altogether, the pre-treatment of the virus followed by inoculation of the treated virus to the cells, pre-treatment of the cells with WDL before viral inoculation and the co-treatment of cells and virus during virus inoculation did not show any promising results. Therefore, they are neither shown nor discussed further.

Interestingly, in the treatment of virus-infected cells during the entire post-inoculation period, we encountered a statistically significant dose-dependent decrease in viral titers (Fig. 4), with a reduction of viral progeny yields in treated cells (at the 40 μM concentration) up to 0.52 Log_{10} units compared to the viral control titers (5.64 Log_{10} units, approximately 10^6 PFU/mL), while at the 20 and 30 μM concentrations, a 0.16 and 0.22 Log_{10} units decrease was observed. An EC_{50} of 18.92 ± 9.4 μM was found, and a selectivity index (SI) of 19.7 (calculated by CC_{50} value divided by the EC_{50} value).

Furthermore, to evaluate the effects of WDL inhibition of OROV replication and post-entry steps, we measured viral progeny yields by plaque formation assays 12, 24, 48 and 72 h post-infection. The results demonstrated that WDL, at a concentration of 40 μM, promoted a more significant inhibition in viral titers from the first 24 h up to 48 h post-
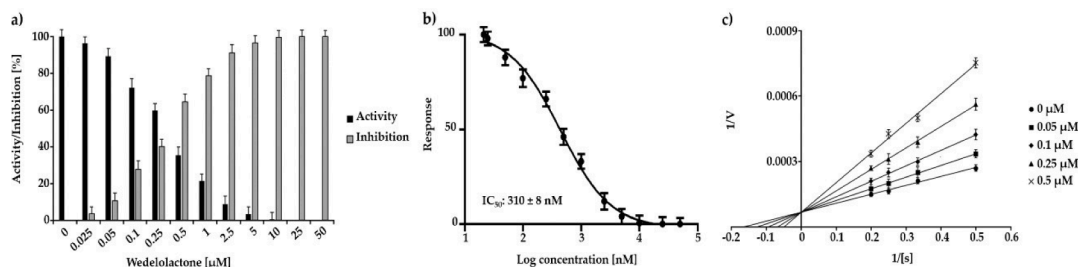
Fig. 2. Inhibition effect of WDL over Endo-Nter domain of OROV followed by dose response curve for IC_{50} determination and inhibition mode of the molecule. (a) Normalised inhibition effect of WDL, (b) the normalised response [%] of Endo-Nter is plotted against the Log of the inhibitor concentration (c) Lineweaver-Burk plot for WDL inhibition of Endo-Nter. Values are shown as the mean $\pm$ standard error obtained from three independent experiments.
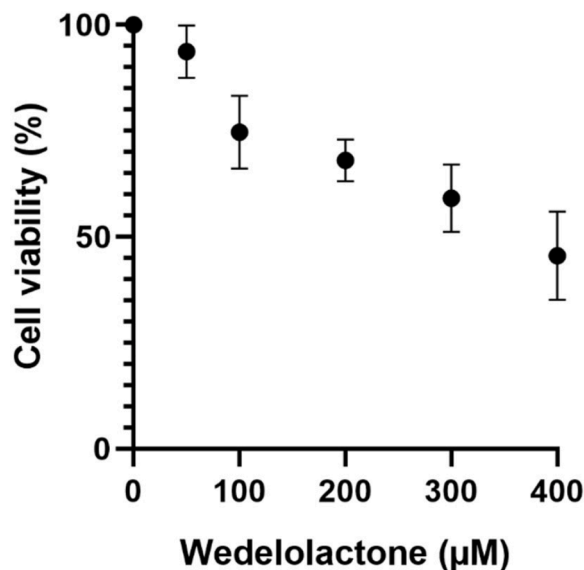

Fig. 3. MTT viability assay for WDL in Vero cells analysed 48 h post-treatment. The *y*-axis represents cell viability in percentages, and the *x*-axis represents the used WDL concentrations ranging from 50 to 400 μM. Values are shown as the mean $\pm$ standard error obtained from three independent experiments. Generated by GraphPad Prism.

infection (Fig. 5), suggesting that WDL can impair OROV replication at an early stage of the viral cycle in a dose-dependent manner and that even at the 72-hour post infection point, some significant inhibitory effects could still be observed.

3.6. In silico studies of the endonuclease N-terminal domain in interaction with WDL

In the absence of a three-dimensional model of the N-terminal region of the OROV endonuclease protein, the structure was modelled using I-TASSER server receiving a C-score of 1.62 (ranging from −5 to 2, with a higher value indicating a high confidence model), which was considered of quality by the MolProbity server. The clashscore (indicating the number of severe steric overlaps per 1000 atoms) gave a value of 3.03 (98th percentile, with the 100th percentile representing the best value among structures with comparable resolution) (Table S1). The Ramachandran plot (Figure S3) showed eight phi/psi angular residuals as outliers, with 86.5 % and 95.5 % of all residuals in preferred and allowed regions, respectively. These results indicate that the protein modelled by I-TASSER has a high-quality conformation suitable for MD simulations. Before performing molecular docking, we carried out 200 ns of MD simulations of the single experimental model of the Endo-Nter domain (3 replicates). The flexibility of the protein structure during the MD simulations was monitored by calculating the RMSD and RMSF
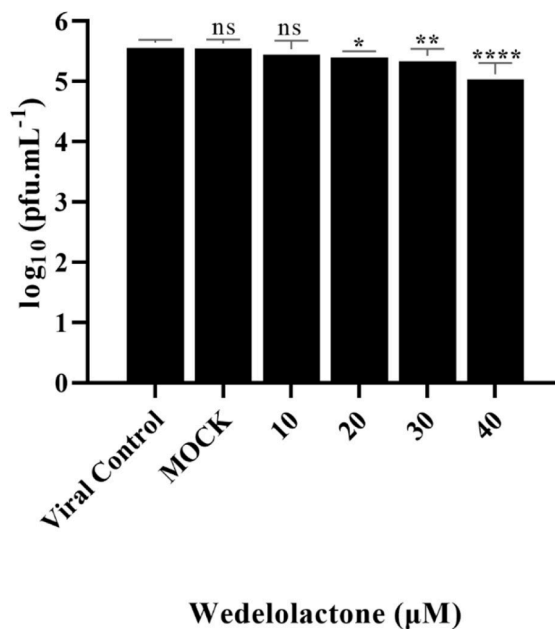
Fig. 4. WDL effect on viral yield is concentration-dependent. OROV production was measured in the presence of several dilutions of the tested compound in Vero cells, with an initial inoculum of MOI 0.1 under post-treatment. PFU infectivity titration of OROV is shown in the left vertical axis. Values are the mean $\pm$ standard error obtained from three independent experiments. Asterisks indicate statistical significance between the control and each group as determined by two-way ANOVA and subsequent Dunnett's test (*, $p < 0.05$/ **, $p < 0.001$/ ****, $p < 0.0001$). Generated by GraphPad Prism.

(Figures S4 and S5). A binding region responsible for the Mn^{2+} ion coordination had been mapped as the active region of the protein (Reguera et al., 2010); based on this information, the WDL was docked in the active site of the Endo-Nter, and three independent runs were performed. The value of the ensemble docking can be visualised in Fig. 6.

Besides the differences in the RMSD plot of the replicates (Figure S6), the Vina score value did not change highly among them.

The lowest (highest) value among replicates ranged from −9.3 kcal/mol to −8.3 kcal/mol (from −5.7 kcal/mol to −5.3 kcal/mol). The binding mode of each selected complex (best and worst Vina scores from each replicate) for the further protein-ligand MD simulations is shown in the right of Fig. 6. The −9.3 kcal/mol complex of replicate 1 was excluded since this frame appeared before RMSD stabilisation (which occurred after 25 ns – frame 250). Note that for all complexes, WDL (yellow stick) was docked in the region of the Mn^{2+} binding site (green sphere) (Fig. 6).

Replicate 1 has the lowest Vina binding affinity score, while replicate 2 has the highest score among the replicates (Table 1).

If we rank the lowest (highest) scores, we get the following order:
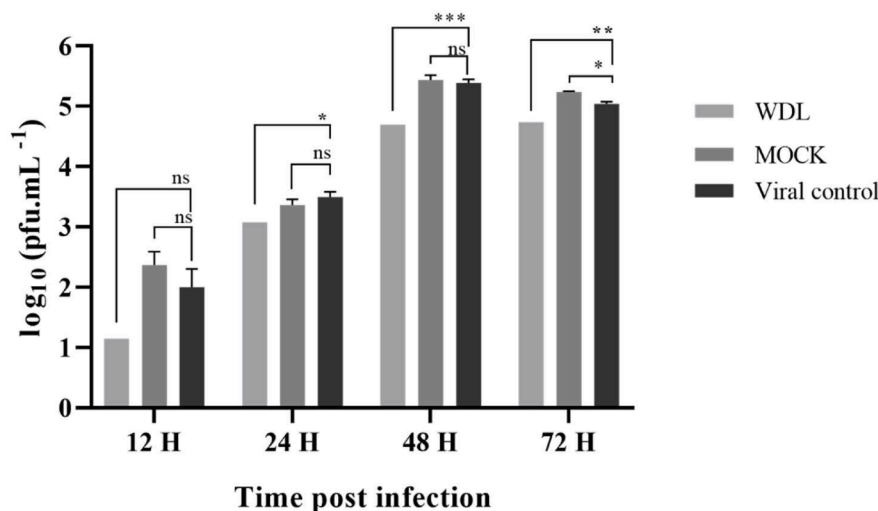
Fig. 5. WDL affects viral progeny production. Antiviral effects of WDL (40 μM) against OROV (MOI = 0.1) infection. Vero cells were infected with OROV and treated with WDL. Culture supernatants were harvested at 12, 24, 48 and 72 hpi and OROV progeny yields were measured through plaque-forming assays. Values are the mean ± standard error obtained from three independent experiments. Asterisks indicate statistical significance between the control and each group as determined by two-way ANOVA and subsequent Dunnett's test (ns, not significant/ *, $p < 0.05$/ **, $p < 0.001$/ ***, $p < 0.0005$). MOCK: cells treated only with DMSO; Viral control: OROV infected cells; WDL: cells infected with OROV and treated with Wedelolactone. Generated by GraphPad Prism.
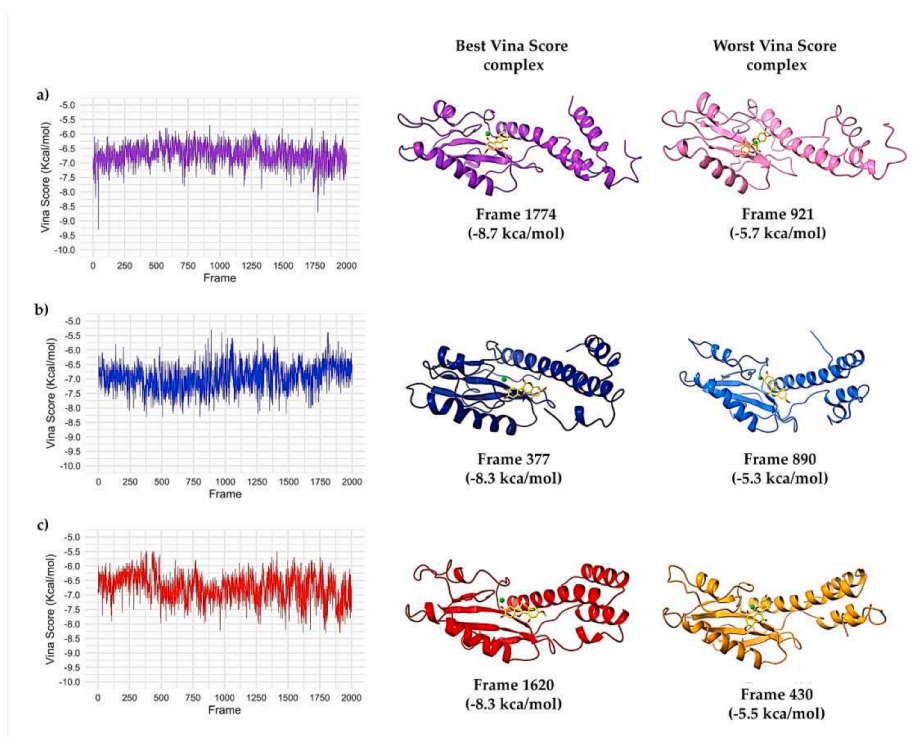
Fig. 6. Ensemble docking with the 2000 frames of each replicates using Vina software. (**a**) Replicate 1 followed by the 3D model representing the best (purple ribbon) and the worst (pink ribbon) Vina score. (**b**) Replicate 2 followed by the 3D model representing the best (dark blue ribbon) and the worst (light blue ribbon) Vina score. (**c**) Replicate 3 followed by the 3D model representing the best (red ribbon) and worst (orange ribbon) Vina score. Mn^{+2} is shown as a green sphere and the WDL molecule as a yellow stick.

replicate 1 < replicate 2 = replicate 3 (replicate 1 < replicate 3 < replicate 2). These values of Vina score are consistent with studies that have used Vina Docking as the previous step for MD of protein-ligand complexes (Anbarasu and Jayanthi, 2018; Malik et al., 2021; Sharma et al., 2022).

The complexes with the best and the worst Vina score of each replicate were selected to be subjected to MD simulations for further free energy analysis. RMSD and RMSF analyses of the Endo-Nter/WDL

complexes were performed (Figures S5-S7), and using the last 50 ns (500 frames), we determined whether the interaction between protein and ligand was favourable and stable in solution through MM/PB(GB)SA analysis. Table 2 summarises the complexes' average binding free energy values (ΔG$_{binding}$).

Regardless of the calculation method (PB or GB), all complexes have a negative binding free energy value, which indicates that all complexes possess stable and favourable ΔG$_{binding}$ during the MD simulation.

Table 1
Vina docking results in kcal/mol.

Replicate	Min	1st quartile	Median	Mean	3rd quartile	Max	Sd[†]
1	−9.3	−6.9	−6.7	−6.7	−6.5	−5.7	0.36
2	−8.3	−7.3	−6.9	−6.93	−6.6	−5.3	0.47
3	−8.3	−7.1	−6.7	−6.74	−6.4	−5.5	0.48

Sd[†] = standard deviation.

Table 2
MM/PB(GB)SA results.

Replicate	MM/PBSA[‡]		MM/GBSA[‡]	
	Complex with Best Vina Scores[†]	Complex with Worst Vina Scores[†]	Complex with Best Vina Scores[†]	Complex with Worst Vina Scores[†]
1	−16.40 ± 2.43	−20.09 ± 1.71	−34.07 ± 3.63	−13.41 ± 2.53
2	−17.32 ± 2.57	−14.86 ± 3.20	−17.62 ± 3.56	−10.70 ± 4.18
3	−14.34 ± 4.18	−22.78 ± 2.57	−30.53 ± 4.97	−15.30 ± 2.63

[‡] Average ± standard deviation.
[†] The best score is the lower Vina score, and the worst is the higher one.

Figure S8 shows the energy per frame of the MM/PBSA analysis.

Per residue decomposition analysis (Fig. 7) of the complexes with the best Vina scores (Fig. 6) shows that for replicate 1 (Fig. 7a), the residues contributing most to the attractive binding energy (less than −0.5 kcal/mol) are: Asn51, Thr75, Asp77, Phe91, and Lys92. For replicate 2 (Fig. 7b), using the same threshold, the residues are Phe73, Asp77, Asp90, Lys92, The103, and Lys106. Finally, for replicate 3 (Fig. 7c), we

highlight residues His34 and Thr75.

Supplementary Table S2 describes the common residues by MM/PBSA analysis observed to sustain their participation in the interactions throughout the simulated trajectory.

Furthermore, the binding mode with the lowest $\Delta G_{binding}$ complex for each replica is presented in Fig. 7 (center and right panels). Note that WDL is located near the Mn^{2+}ion, indicating that the ligand was preserved in the region where it was docked. The interaction between the protein and the ligand is done mainly by van der Waals interactions and hydrogen bonds (Fig. 7, middle and right panel).

In the complexes obtained from frames with worst values of Vina score (Fig. 8), it was observed that for replicate 1, the residues that contributed the most (binding energy $< −0.5$ kcal/mol) were Lys92, Ile102, and Lys106, and for replicate 2, residues Arg39 and Tyr 49. For replicate 3, several residues contributed to the interaction, which reflected the lowest average $\Delta G_{binding}$ (−22.78 kcal/mol). Here we highlight the residues Lys92, Ser99, Ile102, Thr 103, and Ile110. Among the three replicates, Table S2 describes the common residues MM/PBSA analysis.

In the ribbon-stick representation of the complexes in Fig. 8 (center panel), it can be seen that the ligand is slightly distant from the Mn^{2+} ion, the original docking pose, assuming that the fluctuation during the MD simulation happened to form alternate stabilising interaction. As observed earlier, the 2D interactions (Fig. 8, right panel) show that most residues interact through van der Waals and hydrogen bonds for replicates 1 and 2. However, replicate 3 highlights the pi-alkyl/alkyl interactions between the ligand and residues Tyr107, Ile 110, and Phe111.

4. Discussion

No antiviral therapies or vaccines are currently approved for the
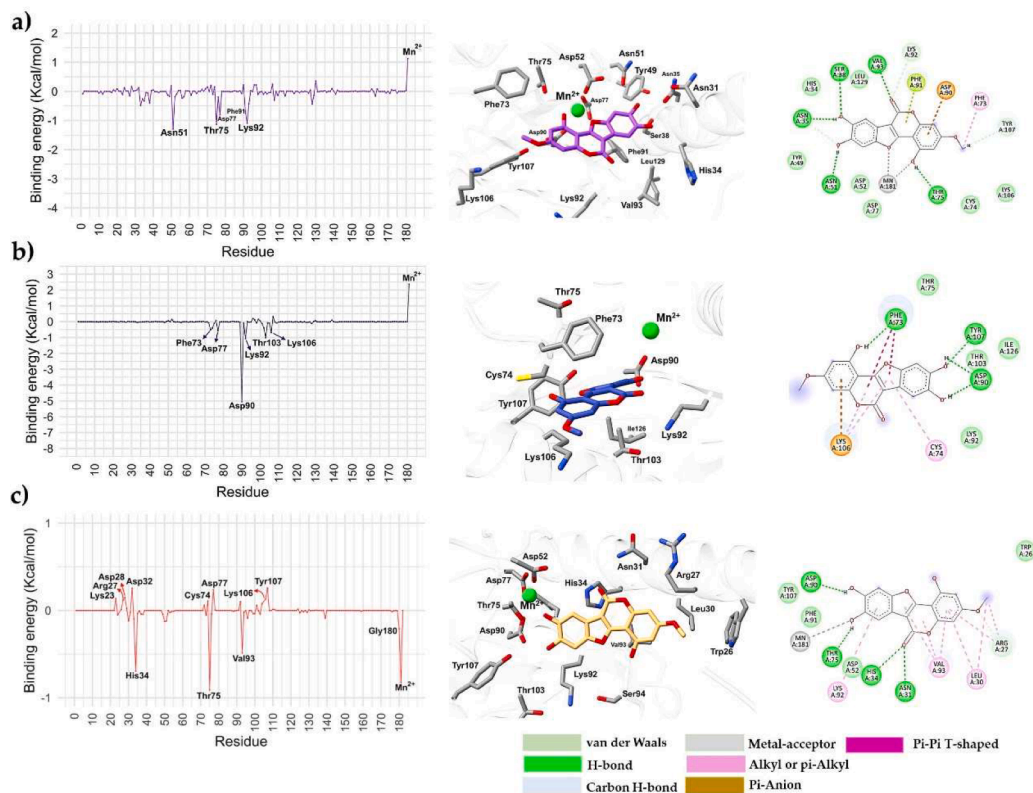
Fig. 7. Per residue decomposition of the binding energy of the Endo-Nter/WDL complex of three independent replicates with the best Vina score (left panel). The 3D ligand binding representation (< 5 Å) is shown in the middle panel (residues are represented as a grey stick of the WDL molecule as a pink, blue, and yellow stick, respectively). The right panel shows the 2D interaction. (**a**) replicate one, (**b**) replicate two, and (**c**) replicate three. Residues are numbered according to the protein sequence, and Mn^{2+} is shown as a green sphere.
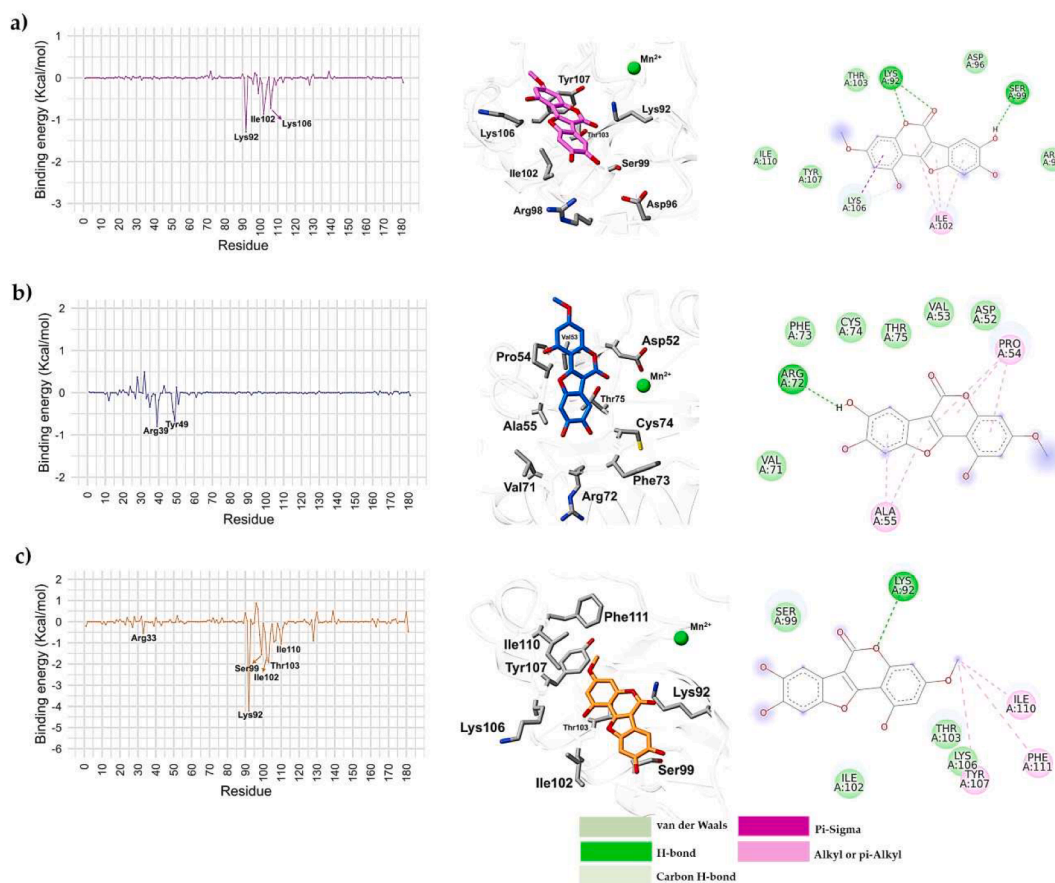
Fig. 8. Per residue decomposition of the binding energy of the Endo-Nter/WDL complex of three independent replicates with the worst Vina score (left panel). The 3D ligand binding representation ($<$ 5 Å) is shown in the centre panel (residues are represented as a grey stick of the WDL molecule as a pink, blue, and yellow stick, respectively). The right panel shows the 2D interaction. (a) Replicate one, (b) replicate two, and (c) replicate three. Residues are numbered according to the protein sequence, and Mn2+ is shown as a green sphere.

treatment or prevention of OROV. The successive OROV outbreaks in South America (Mourão et al., 2009; Romero-Alvarez and Escobar, 2018, 2017; Sakkas et al., 2018), the latest being in French Guiana (Gaillet et al., 2021), have highlighted the urgent need for such medical countermeasures. Here, we report that Wedelolactone (7-methoxy 5,11, 12-trihydroxy-coumestan), a natural coumestan derived from *Eclipta prostrata* with known medical properties such as hepatoprotective (Qingqiong et al., 2018; Xia et al., 2013; Zhao et al., 2015), antivenom (Melo et al., 2010; Melo and Ownby, 1999), anti-cancer (Hsieh et al., 2015; Sarveswaran et al., 2016, 2012), antioxidant (Li et al., 2020; Mao-mao et al., 2019), anti-inflammatory (Mao-mao et al., 2019; Yuan et al., 2013), anti-diabetics (Shahab and Ahmad, 2018), and also neuro, cardio and osteoprotective (Liu et al., 2016; Peng et al., 2017; Sharma et al., 2021). Besides its inhibitory effects of viral proteins (HIV integrase and HCV RNA dependent RNA polymerase), as well as immediate early and some later viral replication steps of HCMV, in our study, WDL inhibited the replication of OROV in cell culture, and here we proposed the interaction with the N-teminal region of the viral polymerase.

The results report the first effects of WDL on a member of the *Peribunyaviridae* family. Here we demonstrate that WDL had antiviral activity in infected Vero cell culture as early as the first 12 h post viral inoculation and up to 48 h post infection and incubation with the molecule, with reduction of viral progeny yields, which demonstrates impairment of replication steps in cells such as viral genome replication, protein synthesis, assembly and release (Acrani et al., 2010), and even mild inhibitory effects at the 72-hour time point, where the reduced inhibitory effects is probably due to cell metabolisation of the molecule.

Furthermore, WDL also and inhibited OROV endonucleases directly in an *in vitro* assay. *In vitro* and *in silico* studies demonstrate the anti-OROV activity of WDL, which is associated with viral endonuclease inhibition. Considering all the residues with negative energy contribution, we determined that 12 residues are common in the complexes obtained from frames with best and worst Vina scores (Arg33, Asn35, Tyr36, Phe37, Asn51, Ile89, Val95, Ile102, Thr103, Val125, Ile126, and Arg128). It is important to highlight that, except for replicas 2 (from the complex with the worst Vina score) and 3 (from the complex with the best Vina score), Lys92 and/or Lys106 appear as the negative energy residues. These residues are known to be putative catalytic lysines located near the active site (Kilian et al., 2013; Reguera et al., 2010). Studies have suggested that an alanine mutation in these residues leads to the elimination or reduction of endonuclease activity, likely due to reduced RNA binding from the loss of the positively charged side chain of the lysine (Reguera et al., 2010). Thus, if WDL interacts in this protein region with high affinity and stability, it is expected to limit RNA access and binding and promote endonuclease inhibition.

5. Conclusion and future perspectives

Over half a million people are estimated to have been infected with OROV. It is assumed that the incidence and disease burden of OROV is underestimated due to the similarity of its clinical presentation to febrile illnesses caused by other arboviruses, such as Dengue, Zika, Chikungunya, and Yellow Fever. Many cases of infection indicate the importance of pursuing new small molecule-based therapeutics to combat emerging

viral pathogens. Among these, inhibitors against OROV, an emerging viral pathogen of orthobunyavirus genera, represent a critical unmet medical need. In that regard, endonuclease inhibitors of OROV are attractive targets for antiviral drug development. Wedelolactone possessed significant antiviral activity, based on the obstruction of viral endonuclease pocket, inducing a minor quantity formation of virus progeny. Thus, this molecule is a promising lead molecule against OROV. However, further investigation is needed to explore the antiviral mechanism and stability of the molecule in animal models.

CRediT authorship contribution statement

Rafaela dos Santos Peinado: Conceptualization, Methodology, Formal analysis, Data curation, Writing – original draft, Writing – review & editing. **Marielena Vogel Saivish:** Conceptualization, Methodology, Formal analysis, Data curation, Writing – original draft, Writing – review & editing. **Gabriela de Lima Menezes:** Methodology, Formal analysis, Writing – original draft, Writing – review & editing. **Umberto Laino Fulco:** Formal analysis, Writing – review & editing. **Roosevelt Alves da Silva:** Formal analysis, Writing – review & editing, Methodology. **Karolina Korostov:** Writing – review & editing. **Raphael Josef Eberle:** Methodology, Writing – review & editing, Resources. **Paulo A. Melo:** Writing – review & editing. **Maurício Lacerda Nogueira:** Resources, Funding acquisition, Writing – review & editing. **Carolina Colombelli Pacca:** Supervision, Resources, Writing – review & editing. **Raghuvir Krishnaswamy Arni:** Project administration, Funding acquisition, Writing – review & editing. **Mônika Aparecida Coronado:** Conceptualization, Methodology, Resources, Supervision, Project administration, Funding acquisition, Writing – review & editing.

Declaration of competing interest

The authors declare that they have no known competing financial interests or personal relationships that could have appeared to influence the work reported in this paper.

Data availability

Data will be made available on request.

Acknowledgements

Supplementary materials

Supplementary material associated with this article can be found, in the online version, at doi:10.1016/j.crmicr.2024.100238.

References

Abraham, M.J., Murtola, T., Schulz, R., Páll, S., Smith, J.C., Hess, B., Lindahl, E., 2015. GROMACS: high performance molecular simulations through multi-level parallelism from laptops to supercomputers. SoftwareX. 1–2, 19–25. https://doi.org/10.1016/j.softx.2015.06.001.

Acrani, G.O., Gomes, R., Proença-Módena, J.L., da Silva, A.F., Oliveira Carminati, P., Silva, M.L., Santos, R.I.M., Arruda, E., 2010. Apoptosis induced by Oropouche virus infection in HeLa cells is dependent on virus protein expression. Virus. Res. 149, 56–63. https://doi.org/10.1016/j.virusres.2009.12.013.

Amroun, A., Priet, S., de Lamballerie, X., Quérat, G., 2017. Bunyaviridae RdRps: structure, motifs, and RNA synthesis machinery. Crit. Rev. Microbiol. 43, 753–778. https://doi.org/10.1080/1040841X.2017.1307805.

Anbarasu, K., Jayanthi, S., 2018. Identification of curcumin derivatives as human LMTK3 inhibitors for breast cancer: a docking, dynamics, and MM/PBSA approach. 3 Biotech 8. 10.1007/s13205-018-1239-6.

Anderson, C.R., Spence, L., Downs, W.G., Aitken, T.H., 1961. Oropouche virus: a new human disease agent from Trinidad, West Indies. Am. J. Trop. Med. Hyg. 104.

Berendsen, H.J.C., Postma, J.P.M., van Gunsteren, W.F., DiNola, A., Haak, J.R., 1984. Molecular dynamics with coupling to an external bath. J. Chem. Phys. 81, 3684–3690. https://doi.org/10.1063/1.448118.

Billecocq, A., Sipegel, M., Vialat, P., Kohl, A., Weber, F., Bouloy, M., Haller, O., 2004. NSs protein of rift valley fever virus blocks interferon production by inhibiting host gene transcription. J. Virol. 78, 9798–9806. https://doi.org/10.1128/jvi.78.18.9798-9806.2004.

Gaillet, M., Pichard, C., Restrepo, J., Lavergne, A., Perez, L., Enfissi, A., Abboud, P., Lambert, Y., Ma, L., Monot, M., Demar, M., Djossou, F., Servas, V., Nacher, M., Andrieu, A., Prudhomme, J., Michaud, C., Rousseau, C., Jeanne, I., Duchemin, J.B., Epelboin, L., Rousset, D., 2021. Outbreak of Oropouche virus in French guiana. Emerg. Infect. Dis. 27, 2711–2714. https://doi.org/10.3201/eid2710.204760.

Gerrard, S.R., Bird, B.H., Albariño, C.G., Nichol, S.T., 2007. The NSm proteins of Rift Valley fever virus are dispensable for maturation, replication and infection. Virology. 359, 459–465. https://doi.org/10.1016/j.virol.2006.09.035.

Guo, Y., Wang, W., Ji, W., Deng, M., Sun, Y., Zhou, H., Yang, C., Deng, F., Wang, H., Hu, Z., Lou, Z., Rao, Z., 2012. Crimean–Congo hemorrhagic fever virus nucleoprotein reveals endonuclease activity in bunyaviruses. Proc Natl Acad Sci U.S.A 109, 5046–5051. https://doi.org/10.1073/pnas.1200808109.

Hess, B., Bekker, H., Berendsen, H.J.C., Fraaije, J.G.E.M., 1997. LINCS: a linear constraint solver for molecular simulations. J. Comput. Chem. 18, 1463–1472. https://doi.org/10.1002/(SICI)1096-987X(199709)18:12<1463::AID−JCC4>3.0.CO;2-H.

Hockney, R.W., Goel, S.P., Eastwood, J.W., 1974. Quiet high-resolution computer models of a plasma. J. Comput. Phys. 14, 148–158. https://doi.org/10.1016/0021-9991(74)90010-2.

Hou, T., Wang, J., Li, Y., Wang, W., 2011. Assessing the performance of the MM/PBSA and MM/GBSA Methods. 1. The accuracy of binding free energy calculations based on molecular dynamics simulations. J. Chem. Inf. Model. 51, 69–82. https://doi.org/10.1021/ci100275a.

Hsieh, C., Kuo, P., Hou, M., Hung, J., Chang, F., 2015. Wedelolactone inhibits breast cancer-induced osteoclastogenesis by decreasing Akt /mTOR signaling. Int. J. Oncol. 46, 555–562. https://doi.org/10.3892/ijo.2014.2769.

Hutter, J., 2012. Car-Parrinello molecular dynamics. Wiley. Interdiscip. Rev. Comput. Mol. Sci. 2, 604–612. https://doi.org/10.1002/wcms.90.

Kilian, P., Valdes, J.J., Lecina-Casas, D., Chrudimský, T., Růžek, D., 2013. The variability of the large genomic segment of Tahyňa orthobunyavirus and an all-atom exploration of its anti-viral drug resistance. Infect. Genet. Evol. 20, 304–311. https://doi.org/10.1016/j.meegid.2013.09.023.

Kumar, P., Nagarajan, A., Uchil, P.D., 2018. Analysis of Cell Viability By the MTT Assay. Cold Spring Harb Protoc. https://doi.org/10.1101/pdb.prot095505, 2018pdb.prot095505.

Lennette, E.H., 1995. Diagnostic procedures for viral, rickettsial, and chlamydial infections, 7th ed. Am J Public Health, Washington DC.

Li, X., Wang, T., Liu, J., Liu, Y., Zhang, J., Lin, J., Zhao, Z., Chen, D., 2020. Effect and mechanism of wedelolactone as antioxidant-coumestan on OH-treated mesenchymal stem cells. Arab. J. Chem. 13, 184–192. https://doi.org/10.1016/j.arabjc.2017.03.008.

Liu, Y., Han, X., Bo, J., Ma, H., Rollinger, J.M., Stern, P.H., 2016. Wedelolactone enhances osteoblastogenesis but inhibits osteoclastogenesis through Sema3A/NRP1/PlexinA1 Pathway. Front. Pharmacol. 7, 375. https://doi.org/10.3389/fphar.2016.00375.

Malik, A., Naz, A., Ahmad, S., Hafeez, M., Awan, F.M., Jafar, T.H., Zahid, A., Ikram, A., Rauff, B., Hassan, M., 2021. Inhibitory potential of phytochemicals on interleukin-6-mediated T-cell reduction in COVID-19 patients: a computational approach. Bioinform. Biol. Insights. 15 https://doi.org/10.1177/11779322211021430.

Manvar, D., Mishra, M., Kumar, S., Pandey, V.N., 2012. Identification and evaluation of anti Hepatitis C Virus phytochemicals from Eclipta alba. J. Ethnopharmacol. 144, 545–554. https://doi.org/10.1016/j.jep.2012.09.036.Identification.

Mao-mao, Z., Long, W., Dang, Y., Chang, L., Shi-ting, P., Xing-hua, L., Ru, L., 2019. Wedelolactone alleviates doxorubicin-induced inflammation and oxidative stress damage of podocytes by IκK/IκB/NFκB pathway. Biomed. PharmacOther 117, 1–7. https://doi.org/10.1016/j.biopha.2019.109088.

Melo, P.A., Ownby, C.L., 1999. Ability of wedelolactone, heparin, and para-bromophenacyl bromide to antagonise the myotoxic effects of two crotaline venoms

and their PLA2 myotoxins. Toxicon. 37, 199–215. https://doi.org/10.1016/S0041-0101(98)00183-4.

Melo, P.A., Pinheiro, D.A., Ricardo, H.D., Fernandes, F.F.A., Tomaz, M.A., El-Kik, C.Z., Strauch, M.A., da Fonseca, T.F., Sifuentes, D.N., Calil-Elias, S., Buarque, C.D., Brito, F.V., Costa, P.R.R., Da Silva, A.J.M., 2010. Ability of a synthetic coumestan to antagonise Bothrops snake venom activities. Toxicon. 55, 488–496. https://doi.org/10.1016/j.toxicon.2009.09.021.

Mourão, M.P.G., Bastos, M.S., Gimaque, J.B.L., Mota, B.R., Souza, G.S., Grimmer, G.H.N., Galusso, E.S., Arruda, E., Figueiredo, L.T.M., 2009. Oropouche Fever Outbreak, Manaus, Brazil, 2007–2008. Emerg. Infect. Dis. 15, 2063–2064. https://doi.org/10.3201/eid1512.090917.

Nguyen, H., Roe, D.R., Simmerling, C., 2013. Improved generalized born solvent model parameters for protein simulations. J. Chem. Theory. Comput. 9, 2020–2034. https://doi.org/10.1021/ct3010485.

Noble, E., Cox, A., Deval, J., Kim, B., 2012. Endonuclease substrate selectivity characterised with full-length PA of influenza A virus polymerase. Virology. 433, 27–34. https://doi.org/10.1016/j.virol.2012.07.008.

O'Boyle, N.M., Banck, M., James, C.A., Morley, C., Vandermeersch, T., Hutchison, G.R., 2011. Open Babel: an open chemical toolbox. J. Cheminform. 3, 33. https://doi.org/10.1186/1758-2946-3-33.

Olsson, M.H.M., Søndergaard, C.R., Rostkowski, M., Jensen, J.H., 2011. PROPKA3: consistent treatment of internal and surface residues in empirical pK_a Predictions. J. Chem. Theory. Comput. 7, 525–537. https://doi.org/10.1021/ct100578z.

Peng, L., Huang, X., Jin, X., Jing, Z., Yang, L., Zhou, Y., Ren, J., Zhao, Y., 2017. Wedelolactone, a plant coumarin, prevents vascular smooth muscle cell proliferation and injury-induced neointimal hyperplasia through Akt and AMPK signaling. Exp. Gerontol. 96, 73–81. https://doi.org/10.1016/j.exger.2017.06.011.

Pettersen, E.F., Goddard, T.D., Huang, C.C., Couch, G.S., Greenblatt, D.M., Meng, E.C., Ferrin, T.E., 2004. UCSF Chimera - A visualisation system for exploratory research and analysis. J. Comput. Chem. 25, 1605–1612. https://doi.org/10.1002/jcc.20084.

Pettersen, E.F., Goddard, T.D., Huang, C.C., Meng, E.C., Couch, G.S., Croll, T.I., Morris, J. H., Ferrin, T.E., 2021. UCSF ChimeraX: structure visualisation for researchers, educators, and developers. Protein Sci. 30, 70–82. https://doi.org/10.1002/pro.3943.

Qingqiong, L., Ding, J., Zhu, P., Chen, F., Xu, L., 2018. Hepatoprotective effect of wedelolactone against concanavalin a-induced liver injury in Mice. Am. J. Chin. Med. (Gard City N. Y.) 46, 1–15. https://doi.org/10.1142/S0192415X1850043X.

Reguera, J., Weber, F., Cusack, S., 2010. Bunyaviridae RNA polymerases (L-Protein) have an N-Terminal, Influenza-like endonuclease domain, essential for viral cap-dependent transcription. PLoS. Pathog. 6, e1001101 https://doi.org/10.1371/journal.ppat.1001101.

Romero-Alvarez, D., Escobar, L.E., 2018. Oropouche fever, an emergent disease from the Americas. Microbes. Infect. 20, 135–146. https://doi.org/10.1016/j.micinf.2017.11.013.

Romero-Alvarez, D., Escobar, L.E., 2017. Vegetation loss and the 2016 Oropouche fever outbreak in Peru. Mem. Inst. Oswaldo Cruz. 112, 292–298. https://doi.org/10.1590/0074-02760160415.

Roy, A., Lim, L., Srivastava, S., Lu, Y., Song, J., 2017. Solution conformations of Zika NS2B-NS3pro and its inhibition by natural products from edible plants. PLoS. One 12, e0180632. https://doi.org/10.1371/journal.pone.0180632.

Sakkas, H., Bozidis, P., Franks, A., Papadopoulou, C., 2018. Oropouche fever: a review. Viruses. 10, 1–16.

Sarveswaran, S., Gautam, S.C., Ghosh, J., 2012. Wedelolactone, a medicinal plant-derived coumestan, induces caspase-dependent apoptosis in prostate cancer cells via

downregulation of PKC ε without inhibiting Akt. Int. J. Oncol. 41, 2191–2199. https://doi.org/10.3892/ijo.2012.1664.

Sarveswaran, S., Ghosh, R., Parikh, R., Ghosh, J., 2016. Wedelolactone, an anti-inflammatory botanical, interrupts c-Myc oncogenic signaling and synergises with enzalutamide to induce apoptosis in prostate cancer cells. Mol. Cancer Ther. 15, 2791–2801. https://doi.org/10.1158/1535-7163.MCT-15-0861.Wedelolactone.

Shahab, U., Ahmad, S., 2018. Impact of wedelolactone in the anti-glycation and anti-diabetic activity in experimental diabetic animals. IUBMB Life 70, 547–552. https://doi.org/10.1002/iub.1744.

Sharma, A., Vora, J., Patel, D., Sinha, S., Jha, P.C., Shrivastava, N., 2022. Identification of natural inhibitors against prime targets of SARS-CoV-2 using molecular docking, molecular dynamics simulation and MM-PBSA approaches. J. Biomol. Struct. Dyn. 40, 3296–3311. https://doi.org/10.1080/07391102.2020.1846624.

Sharma, S., Trivedi, S., Pandey, T., Ranjan, S., Trivedi, M., Pandey, R., 2021. Wedelolactone mitigates parkinsonism via alleviating oxidative stress and mitochondrial dysfunction through NRF2 /SKN-1. Mol. Neurobiol. 58, 65–77.

Silva, D., Vranken, B.F., 2012. ACPYPE-AnteChamber PYthon Parser interfacE. Res. Notes 5, 367.

Svrlanska, A., Ruhland, A., Marschall, M., Reuter, N., 2020. Wedelolactone inhibits human cytomegalovirus replication by targeting distinct steps of the viral replication cycle. Antiviral Res. 174, 13–35. https://doi.org/10.1016/j.antiviral.2019.104677.

Tewtrakul, S., Subhadhirasakul, S., Cheenpracha, S., Karalai, C., 2007. HIV-1 Protease and HIV-1 Integrase Inhibitory Substances from Eclipta prostrata. PhytOther Res. 21, 1092–1095. https://doi.org/10.1002/ptr.

Travassos da Rosa, J.F., de Souza, W.M., Pinheiro, F.P., Figueiredo, M.L., Cardoso, J.F., Acrani, G.O., Nunes, M.R.T., 2017. Oropouche virus: clinical, epidemiological, and molecular aspects of a neglected orthobunyavirus. Am. J. Trop. Med. Hyg. 96, 1019–1030. https://doi.org/10.4269/ajtmh.16-0672.

Trott, O., Olson, A.J., 2009. AutoDock Vina: improving the speed and accuracy of docking with a new scoring function, efficient optimisation, and multithreading. J. Comput. Chem. NA-NA. https://doi.org/10.1002/jcc.21334.

Valdés-Tresanco, M.S., Valdés-Tresanco, M.E., Valiente, P.A., Moreno, E., 2021. gmx_MMPBSA: a new tool to perform end-state free energy calculations with GROMACS. J. Chem. Theory. Comput. 17, 6281–6291. https://doi.org/10.1021/acs.jctc.1c00645.

Vasconcelos, H.B., Nunes, M.R.T., Casseb, L.M.N., Carvalho, V.L., da Silva, E.V.P., Silva, M., Casseb, S.M.M., Vasconcelos, P.F.C., 2011. Molecular epidemiology of Oropouche Virus. Brazil. Emerg. Infect. Dis. 17, 800–806. https://doi.org/10.3201/eid1705.101333.

Williams, C.J., Headd, J.J., Moriarty, N.W., Prisant, M.G., Videau, L.L., Deis, L.N., Verma, V., Keedy, D.A., Hintze, B.J., Chen, V.B., Jain, S., Lewis, S.M., Arendall, W.B., Snoeyink, J., Adams, P.D., Lovell, S.C., Richardson, J.S., Richardson, D.C., 2018. MolProbity: more and better reference data for improved all-atom structure validation. Protein Sci. 27, 293–315. https://doi.org/10.1002/pro.3330.

Xia, Y., Chen, J., Cao, Y., Xu, C., Li, R., Pan, Y., Chen, X., 2013. Wedelolactone exhibits anti- fi brotic effects on human hepatic stellate. Eur. J. Pharmacol. 714, 105–111. https://doi.org/10.1016/j.ejphar.2013.06.012.

Yuan, F., Chen, J., Sun, P., Guan, S., Xu, J., 2013. Wedelolactone inhibits LPS-induced pro-inflammation via NF-kappaB pathway. J. Biomed. Sci. 20, 1–11.

Zhao, Y., Peng, L., Yang, L., Xu, X., Li, W., Luo, X., 2015. Wedelolactone regulates lipid metabolism and improves hepatic steatosis partly by AMPK activation and up-regulation of expression of PPAR α /LPL and LDLR. PLoS. One 10, 1–17. https://doi.org/10.1371/journal.pone.0132720.